The effects of delay on the HKB model of human motor coordination[*]

L. I. Allen[†], T. G. Molnár[‡], Z. Dombóvári[§], and S. J. Hogan[¶]

Abstract. In this paper, we analyse the celebrated Haken-Kelso-Bunz (HKB) model, describing the dynamics of bimanual coordination, in the presence of delay. We study the linear dynamics, stability, nonlinear behaviour and bifurcations of this model by both theoretical and numerical analysis. We calculate in-phase and anti-phase limit cycles as well as quasi-periodic solutions via double Hopf bifurcation analysis and centre manifold reduction. Moreover, we uncover further details on the global dynamic behaviour by numerical continuation, including the occurrence of limit cycles in phase quadrature and 1-1 locking of quasi-periodic solutions.

Key words. Haken-Kelso-Bunz model, motor coordination, delays, bifurcation

MSC codes. 37G15, 37G25, 34C15, 34C23, 34C25, 37N25

1. Introduction. Human motor coordination is the result of complex interactions, at many different time and length scales. One established way to model bimanual coordination is to assume that the fingers or limbs of experimental subjects are oscillators, capable of generating self-sustained periodic motion. Within this approach, the focus is on understanding the observed *relative phase* ϕ of the two oscillators [22]. Stable *in-phase* ($\phi = 0$) synchronisation is usually found to be the simplest to maintain [6], [21], while stable *anti-phase* ($\phi = \pi$) motion [5] and stable *phase-lagged* states can also occur [9], [12].

The Haken-Kelso-Bunz (HKB) coupled oscillator model [15, 23] was originally developed to explain these different types of bimanual synchronisation, and the ways in which they can occur. Since then it has become the bedrock of all subsequent research in this area.

In more recent times, the HKB model has found application elsewhere. Schizophrenia is a mental illness with high prevalence and a scarcity of satisfactory treatments. This has inspired a drive within the research community [35] to develop methods for early diagnosis and preventative intervention.

The mirror game, where two individuals mirror each other's movements, is considered to be a powerful tool for studying coordination dynamics [29]. In experiments based on this principle, Varlet et al. [37] identified peculiar characteristics of the motion of schizophrenic

[†]Population Health Sciences, University of Bristol, United Kingdom (hk19479@bristol.ac.uk).

[‡]Department of Mechanical and Civil Engineering, California Institute of Technology, Pasadena, CA 91125, USA (tmolnar@caltech.edu).

[§]MTA-BME Lendület Machine Tool Vibration Research Group, Department of Applied Mechanics, Faculty of Mechanical Engineering, Budapest University of Technology and Economics, Budapest 1111, Hungary (dombovari@mm.bme.hu).

[¶]Department of Engineering Mathematics, University of Bristol, Bristol BS8 1UB, United Kingdom (s.j.hogan@bristol.ac.uk). Corresponding Author: ORCiD: 0000-0001-6012-6527

31 patients performing simple synchronisation tasks with healthy individuals. In one version of
32 the mirror game, an HKB-driven virtual player [39] participates with a human partner. The
33 analysis of the resulting motion could form the basis of a diagnostic tool for schizophrenia
34 [26], where motor abnormalities are one of the first indicators of the illness.

35   In their work, Varlet et al. [37] pointed out that the standard HKB coupled oscillator
36 model [15] does not accurately describe the observed dynamics of schizophrenia patients
37 unless a delay is included in the coupling term. The resulting *delayed HKB model* [2, 36,
38 38, 40] is the subject of this paper. Our goal is to inform further research into human
39 coordination dynamics where delay is especially prevalent. In particular, we seek to aid
40 the understanding of the delayed HKB equation by providing insight into the underlying
41 dynamic behaviour of the system. Varlet et al. [37] suggest that the delayed HKB equation
42 may be suitable to capture the mirror game whereas the numerical approaches used by
43 Słowiński et al. [34] indicate that the delayed HKB equation may have limited relevance to
44 experimentally observed behaviour. We aim to help clarify the extent of the utility of the
45 delayed HKB model[1].

46   Our paper is organised as follows. Section 2 describes the delayed HKB model of
47 human motor coordination. Section 3 presents linear stability analysis that is verified by
48 numerical results in Section 4. The nonlinear dynamics of the delayed HKB model are
49 analysed, by centre manifold reduction, in Section 5. We compare these theoretical results
50 with numerical continuation in Section 6.

51   **2. The delayed HKB model.** The delayed HKB model [2, 36] is given by

52 (2.1)
$$\ddot{x}_1(t) + \omega^2 x_1(t) = \left(\gamma - \alpha x_1^2(t) - \beta \dot{x}_1^2(t)\right) \dot{x}_1(t)$$
$$+ \left(a + b\left(x_1(t) - x_2\left(t - \tau_1\right)\right)^2\right)\left(\dot{x}_1(t) - \dot{x}_2\left(t - \tau_1\right)\right),$$
$$\ddot{x}_2(t) + \omega^2 x_2(t) = \left(\gamma - \alpha x_2^2(t) - \beta \dot{x}_2^2(t)\right) \dot{x}_2(t)$$
$$+ \left(a + b\left(x_2(t) - x_1\left(t - \tau_2\right)\right)^2\right)\left(\dot{x}_2(t) - \dot{x}_1\left(t - \tau_2\right)\right).$$

53 This model is a pair of coupled second-order delay differential equations (DDEs). The
54 variables $x_1(t)$ and $x_2(t)$ represent the amplitudes[2] of the individual oscillators at time t.
55 The parameter γ is the linear damping coefficient and α, β are nonlinear damping coeffi-
56 cients, also known as the Van der Pol and Rayleigh coefficients, respectively. Parameter
57 a is the linear coupling coefficient and b is the nonlinear coupling coefficient. The pacing
58 frequency ω is physically positive[3]. The time delays τ_1, τ_2 arise from cognitive and physi-
59 ological processes, typically caused by detection and actuation, which can be different for
60 each oscillator. In this paper, we take these two time delays to be equal: $\tau_1 = \tau_2 =: \tau$. We

---

[1]We note that in the analysis by Słowiński et al., various parameters are fixed at values found by Kay
et al. [20] using experiments studying the hand motion of four participants. However, Peper et al. [30]
suggest that not all limbs can be modelled in the same way which motivates a broader investigation of the
parameter space, as presented here.
[2]In the original HKB paper [22], $x_1(t)$ and $x_2(t)$ are the angular displacements of each finger, with
direction defined symmetrically so that $x_1(t) = x_2(t)$ corresponds to in-phase motion.
[3]In [22], pacing was provided by a metronome.

61 remark that the number of parameters in the delayed HKB model (2.1) could be reduced
62 by introducing the scaled time $\tilde{t} = \omega t$, however, hereinafter we rather use functions of t for
63 easier physical interpretation.
64   The delayed HKB model (2.1) has discrete symmetries in its structure: x_1 and x_2, as
65 well as x_1 and $-x_2$ are interchangeable. These symmetries will ultimately result in the
66 existence of in-phase and anti-phase periodic solutions.
67   We begin our analysis of the delayed HKB model (2.1) by first considering the linearized
68 version of the system, given[4] by

69 (2.2)
$$\ddot{x}_1 + \omega^2 x_1 = \gamma \dot{x}_1 + a \left(\dot{x}_1 - \dot{x}_2(t - \tau) \right),$$
$$\ddot{x}_2 + \omega^2 x_2 = \gamma \dot{x}_2 + a \left(\dot{x}_2 - \dot{x}_1(t - \tau) \right).$$

70 We shall show that these equations provide us with an explanation of the fundamental
71 structures observed in numerical computations [36].
72   In [8, eq. (5)], it was shown that the linear HKB equations in the *absence* of delay
73 could be simplified when written in terms of normal modes. We adopt the same approach
74 here, by setting $\eta^{(i)} = x_1 + x_2$ and $\eta^{(a)} = x_1 - x_2$, corresponding to in-phase motion and
75 anti-phase motion respectively, so that (2.2) becomes

76 (2.3)
$$\ddot{\eta}^{(i)} + \omega^2 \eta^{(i)} = \gamma \dot{\eta}^{(i)} + a \left(\dot{\eta}^{(i)} - \dot{\eta}^{(i)}(t - \tau) \right),$$
$$\ddot{\eta}^{(a)} + \omega^2 \eta^{(a)} = \gamma \dot{\eta}^{(a)} + a \left(\dot{\eta}^{(a)} + \dot{\eta}^{(a)}(t - \tau) \right).$$

77   We consider the stability of the trivial solutions (equilibria) $\eta^{(i,a)} = 0$ of (2.3).
78   • If both $\eta^{(i,a)} = 0$ are stable, then the equilibrium $x_1 = x_2 = 0$ of (2.2) must be
79   stable and we will see no oscillations.
80   • When $\eta^{(i)} = 0$ is unstable and $\eta^{(a)} = 0$ is stable, we expect to find stable in-phase
81   limit cycles in the full system (2.1).
82   • When $\eta^{(i)} = 0$ is stable and $\eta^{(a)} = 0$ is unstable, we expect to find stable anti-phase
83   limit cycles in the full system (2.1).
84   Such limit cycles arise because of a Hopf bifurcation, which occurs when changing
85 parameters of the system. If the leading eigenvalues λ cross the imaginary axis in pairs,
86 $\lambda = \pm i\nu$ where $\nu \neq 0$, then, according to an infinite dimensional version of the Hopf
87 Bifurcation Theorem [17], there will be a Hopf bifurcation when the derivative of the
88 eigenvalue λ with respect to a parameter evaluated at $\lambda = i\nu$ is non-zero.
89   Equations (2.3) are uncoupled. Since they only differ by one sign, we can carry out an
90 analysis on the *linear delayed HKB model*, given by

91 (2.4)
$$\ddot{\eta} + \omega^2 \eta = \gamma \dot{\eta} + a \left(\dot{\eta} \mp \dot{\eta}(t - \tau) \right),$$

92 where $\eta = \eta^{(i)}$ corresponds to the minus sign in the last term and $\eta = \eta^{(a)}$ corresponds to
93 the plus sign.

---

[4]To simplify notation, we do not denote the dependence of x_1 and x_2 on time, unless the delay is involved.
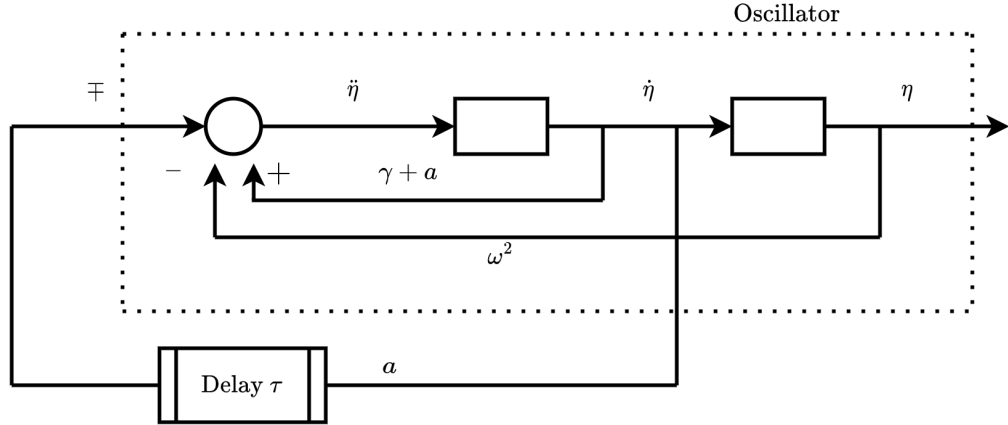
Figure 3.1. *A feedback control system block diagram for the linear delayed HKB model* (3.1). *The damped harmonic oscillator on the left-hand side of* (3.1) *is within the dotted section.*

3. Stability charts for the linear delayed HKB model. In this section we produce stability charts in the (a, τ), (γ, τ) and (γ, a) planes, for arbitrary values of ω, of the trivial solutions of (2.4). These charts will also be used to explain structure of the bifurcation diagram for the nonlinear delayed HKB model (2.1) in the (a, τ) plane produced by Słowiński et al. [36, Figure 2(a)].

Equations (2.4) will be very familiar to control engineers when written in the form:

$$(3.1) \qquad \ddot{\eta}(t) - (\gamma + a)\dot{\eta}(t) + \omega^2 \eta(t) = \mp a\dot{\eta}(t - \tau),$$

The left-hand side of (3.1) represents damped simple harmonic motion, with damping coefficient[5] $-(\gamma + a)$. The right-hand side is a delayed harmonic oscillator with feedback gain $\mp a$, which changes the damping coefficient $-(\gamma + a)$. The feedback control system block diagram is shown in Figure 3.1.

In the absence of delay, the in-phase and anti-phase trivial solutions $\eta^{(i,a)} = 0$ have two lines of Hopf-bifurcations in (a, γ) parameter space; $HB_I : \gamma = 0$ and $HB_A : 2a + \gamma = 0$, see [8, Figure 1]. Bistable regions of these normal modes are also seen.

In the presence of delay, a stability analysis of the equilibrium solution $\eta = 0$ to (3.1) is more complicated, but well established [3, 18, 25]. Details are given in Appendix A.

For the stability chart in (a, τ) parameter space, shown in Figure 3.2, we follow [36] and set[6] $\gamma = 0.641$, $\omega = 2.6\pi$. Regions where $\eta^{(i)} = 0$ is stable are shaded blue, regions where $\eta^{(a)} = 0$ is stable are shaded red. Both $\eta^{(i,a)} = 0$ are stable in the purple regions. The eigenvalues of the in-phase and anti-phase normal modes are denoted by $\lambda^{(i,a)}$ respectively. Stability boundaries occur when the rightmost eigenvalues are pure imaginary: $\lambda^{(i,a)} = i\nu^{(i,a)}$. From (A.6), the sign of the quantity $\rho_\tau = \text{Re}\left(\frac{\partial \lambda}{\partial \tau}\big|_{\lambda=i\nu}\right)$ indicates how the stability of $\eta = 0$ changes as τ increases.

---

[5] We shall consider cases when $-(\gamma + a) \gtrless 0$.

[6] We reproduced their results by setting $\omega = 2\pi(1.3) = 2.6\pi$, suggesting that they took $\omega = 1.3[Hz]$.
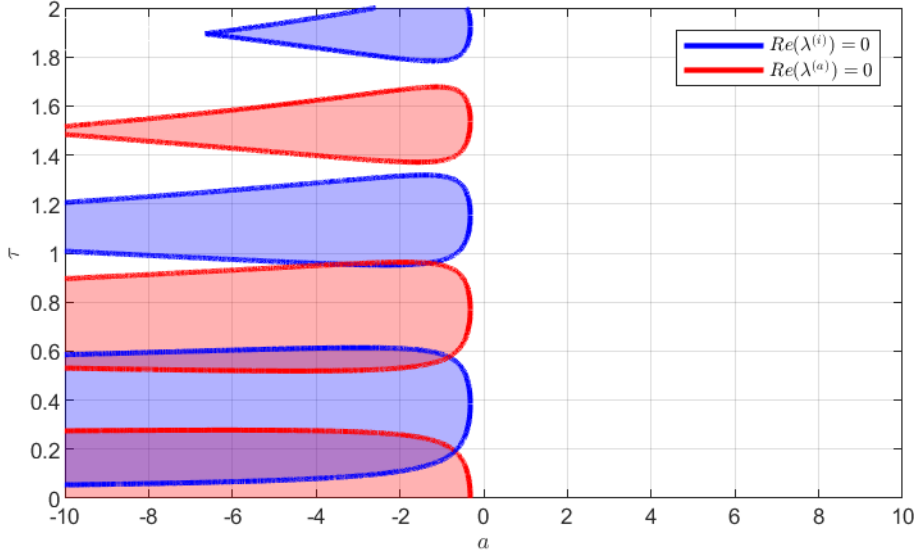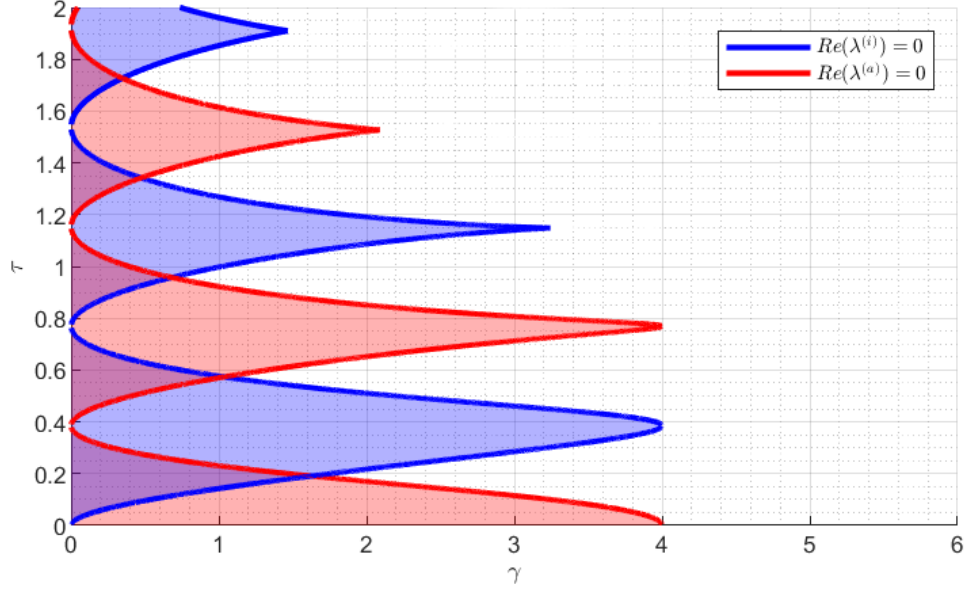
Figure 3.2. *Stability chart in (a, τ) parameter space for the normal modes of the linear delayed HKB equation (3.1) with $\gamma = 0.641$, $\omega = 2.6\pi$. Regions where $\eta^{(i)}$ is stable are shaded blue, regions where $\eta^{(a)}$ is stable are shaded red. The normal modes $\eta^{(i,a)}$ are both stable in the purple regions and both unstable in the white regions.*

In the absence of delay, along the line $\tau = 0$ in Figure 3.2, $\eta^{(a)} = 0$ is stable (and $\eta^{(i)} = 0$ is unstable) for $a < -\gamma/2 = -0.3205$, in agreement with the stability boundary $HB_A : 2a + \gamma = 0$ in [8, Figure 1]. We observe finite amplitude in-phase limit cycles in the full equations (2.1) with $\tau = 0$ [1, 8].

As τ increases for fixed $a < -\gamma/2 = -0.3205$, initially $\eta^{(a)} = 0$ remains stable. Then we observe a number of stability switches. $\eta^{(i)} = 0$ becomes stable on crossing the lowest blue line in Figure 3.2. When both $\eta^{(i,a)} = 0$ are stable (in the purple regions), we have the case when $x_1 = x_2 = 0$ is stable. So, small but finite values of the delay τ eliminate the finite amplitude in-phase limit cycles in (2.1). On crossing the lowest red line in Figure 3.2, $\eta^{(a)} = 0$ loses stability. We expect to see finite amplitude anti-phase limit cycles in the full delayed HKB model (2.1) in the blue region around $\tau = 0.4$ for $a < -\gamma/2 = -0.3205$. Similar observations can be made as we increase τ further in Figure 3.2.

For the stability chart in (γ, τ) parameter space, shown in Figure 3.3, we set $a = -2$ and $\omega = 2.6\pi$ [36]. The colour scheme and the definitions of $\lambda^{(i,a)}$ and $\rho_\tau^{(i,a)}$ are the same as those in Figure 3.2. In Figure 3.3, along the line $\tau = 0$, we see that $\eta^{(a)} = 0$ is stable (and $\eta^{(i)} = 0$ is unstable) for $\gamma < -2a = 4$, in agreement with the stability boundary $HB_A : 2a + \gamma = 0$ in [8, Figure 1]. We see further stability switches as τ increases.

Figures 3.2 and 3.3 show a periodic nature in the stability curves as τ increases. We can explain this observation as follows. In (A.15), we show that when $\tau = \frac{n\pi}{\omega}$, $n \in \mathbb{Z}$, stability boundaries are given by $\gamma = a(\pm(-1)^n - 1)$ for $\omega \neq 0$. When n is even, that means the boundaries are $\gamma = 0$ for $\eta^{(i)}$ and $\gamma + 2a = 0$ for $\eta^{(a)}$. When n is odd, the boundaries are

Figure 3.3. *Stability chart in (γ, τ) parameter space for the normal modes of the linear delayed HKB equation* (3.1) *with* $a = -2$, $\omega = 2.6\pi$. *The colour scheme is the same as that in Figure 3.2.*

138   swapped and given by $\gamma + 2a = 0$ for $\eta^{(i)}$ and $\gamma = 0$ for $\eta^{(a)}$.

139   Stability charts in the (γ, a) plane are illustrated in Figure 3.4, showing how the stability
140   boundaries evolve as τ increases from 0 to π/ω. At $\tau = 0$ the in-phase and anti-phase
141   stability curves are $\gamma = 0$ and $2a + \gamma = 0$ respectively. As τ increases, these boundaries
142   deform and cross, eventually switching when $\tau = \pi/\omega$, as expected.

143   **4. Comparison with numerical stability charts.** Up to now, we have analysed the
144   linear delayed HKB (2.2), which is valid for small amplitudes. However, most experiments
145   are performed in the nonlinear regime. The study by Słowiński et al. [36] is the only
146   bifurcation analysis of the nonlinear delayed HKB model (2.1), but it is entirely numerical,
147   and does not consider the linearised equations. These authors fixed the linear damping
148   coefficient $\gamma = 0.641$ and the nonlinear damping coefficients $\alpha = 12.457$, $\beta = 0.007905$
149   [20]. Variation of the other parameters was considered within the range of experimentally
150   observed values. We follow these authors with the same choice of parameters, with $\omega =$
151   $2\pi(1.3) = 2.6\pi$.

152   Figure 3.3 shows the analytic stability curves in (γ, τ) parameter space. Our own
153   numerical continuation of the Hopf bifurcations using DDE-BIFTOOL [13, 33] shows exact
154   agreement between the numerical and analytic curves (not shown). Since the analytic
155   curves lie exactly on the numerical curves, the generic Hopf bifurcation curves can be
156   deduced exactly from analysis of the linear system (2.2).

157   Figure 3.3 shows that the stability curves satisfy $0 < \gamma < 4$. This can be explained
158   using the analysis in Appendix A. Conditions (A.5) for eigenvalues to touch or cross the
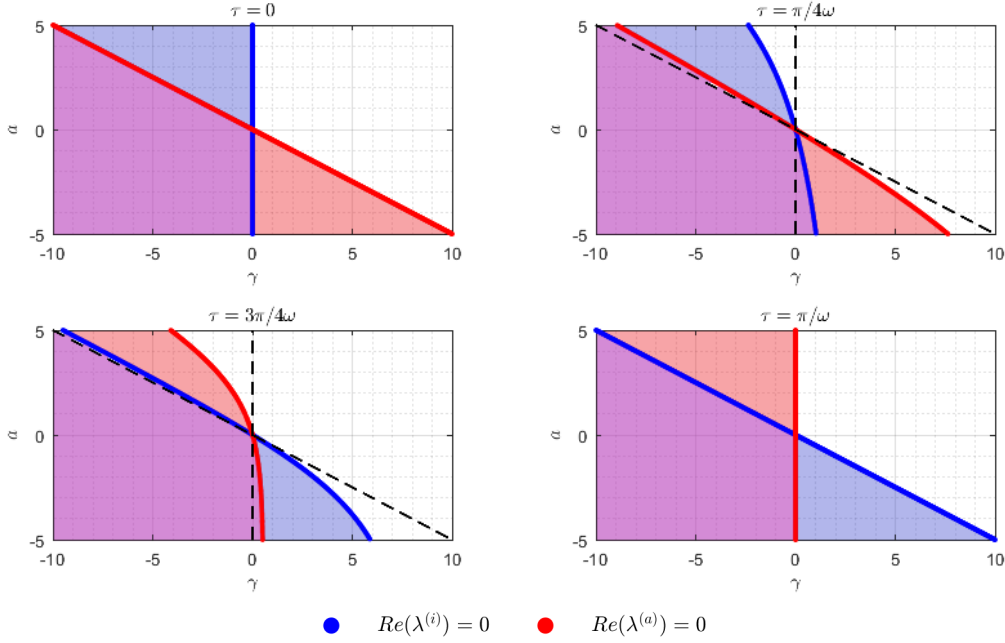
Figure 3.4. *Stability chart in (γ, a) parameter space for the normal modes of the linear delayed HKB equation (3.1), for different values of τ, with $\omega = 2.6\pi$. The colour scheme is the same as that in Figure 3.2. The stability chart with $\tau = 0$ was given in [8, Figure 1], where regions of instability were highlighted. Within the parameter ranges illustrated, the stability boundaries for $\tau = \frac{\pi}{\omega}$ are the same as those for $\tau = 0$, but with the in-phase and anti-phase curves swapped.*

imaginary axis can be combined to give $\gamma(\gamma + 2a) < 0$. Therefore, for $a = -2$ as in Figure 3.3, we have $0 < \gamma < 4$.

Słowiński et al. [36, Figure 2(a)] carried out a comprehensive numerical analysis of the full problem (2.1), using DDE-BIFTOOL. They found many bifurcations in[7] $a > 0$, and torus bifurcations in $a < 0$.

5. Applying centre manifold theory to the delayed HKB equation. A standout observation of Figures 3.2 and 3.3 is the crossing of Hopf bifurcation curves. At such points we expect to find double Hopf (or Hopf-Hopf) bifurcations, as two pairs of eigenvalues cross the imaginary axis at the same time.

We now revert to the full problem (2.1), and investigate the double Hopf points in (a, τ) parameter space, unfolding the in-phase and anti-phase periodic orbits as parameter values are varied nearby. We use centre manifold theory, with symbolic computations in Maple[TM] based on the tutorial codes given in [7]; the details of this calculation are outlined in Appendix B.

Using (A.9) and (A.10), we find four double Hopf bifurcations at $(a, \tau) = (a_c, \tau_c)$ for[8] $a \in [-10, 10]$, $\tau \in (0, 2)$, labelled HH1 to HH4 in Table 5.1, along with values for the critical

---

[7]Experiments tend to suggest that $a < 0$.
[8]This range was given in Figure 3.2.

175 eigenvalues $\lambda^{(i,a)} = \mathrm{i}\nu^{(i,a)}$.

	a_c	τ_c	$\nu^{(i)}$	$\nu^{(a)}$
HH1	-0.68609	0.19214	7.83301	8.51761
HH2	-0.83431	0.57621	8.58402	7.77241
HH3	-1.33683	0.95920	7.61733	8.75879
HH4	-3.37162	0.95457	7.23890	9.21666

Table 5.1
Parameter values for the double Hopf bifurcations in the (a, τ) plane, with $\gamma = 0.641$, $\omega = 2.6\pi$.

176   The normal form of the double Hopf bifurcation can be expressed in polar coordinates,
177 with amplitudes r_1, r_2 (B.30) and phase angles φ_1, φ_2 (B.31); see also [28]. In (B.30), r_1
178 corresponds to eigenvalue $\mathrm{i}\nu^{(i)}$, and r_2 corresponds to eigenvalue $\mathrm{i}\nu^{(a)}$. So, $r_1 \neq 0$, $r_2 = 0$
179 steady states of (B.30) correspond to in-phase limit cycles, and $r_1 = 0$, $r_2 \neq 0$ corresponds
180 to anti-phase limit cycles.

181   Table 5.2 gives values for the normal form coefficients a_{jk} and parameters ρ_{jk}, used
182 in the expressions (B.32) for the unfolding parameters, for each of the four double Hopf
183 points. Note that the normal form coefficients can also be computed for a wide class of
184 time delay systems numerically using the approach proposed in [4] that was implemented
185 as part of DDE-BIFTOOL. In the sequel, we explore the point HH1 in detail.

186   **5.1. Phase portraits.** The normal form for the double Hopf bifurcation (B.30) gives
187 rise to distinct structurally stable phase portraits in different regions of parameter space
188 about the double Hopf points. To see this, we look at the possible steady states of (B.30),

189 (5.1)
$$\begin{aligned}
\textcircled{1}: \quad & (r_1, r_2) = (0, 0), \\[2mm]
\textcircled{2}: \quad & (r_1, r_2) = \left(\sqrt{-\frac{b_1}{a_{11}}}, 0 \right), \\[2mm]
\textcircled{3}: \quad & (r_1, r_2) = \left(0, \sqrt{-\frac{b_2}{a_{22}}} \right), \\[2mm]
\textcircled{4}: \quad & (r_1, r_2) = \left(\sqrt{\frac{a_{12}b_2 - a_{22}b_1}{a_{11}a_{22} - a_{12}a_{21}}}, \sqrt{\frac{a_{21}b_1 - a_{11}b_2}{a_{11}a_{22} - a_{12}a_{21}}} \right).
\end{aligned}$$

190   According to Guckenheimer and Holmes [14], there is a partition of parameter space
191 into regions with topologically different phase portraits in which different combinations of
192 steady states exist simultaneously. The lines separating these regions are given by

193 (5.2)
$$\begin{aligned}
&\text{Line 1:} \quad b_1 = 0, \\
&\text{Line 2:} \quad b_2 = 0, \\
&\text{Line 3:} \quad a_{12}b_2 - a_{22}b_1 = 0, \\
&\text{Line 4:} \quad a_{21}b_1 - a_{11}b_2 = 0.
\end{aligned}$$

	a_{11}	a_{12}	a_{21}	a_{22}	ρ_{11}	ρ_{12}	ρ_{21}	ρ_{22}
HH1	-1.45930	-2.98167	-3.17291	-1.62071	0.41422	-2.53782	0.44713	2.99651
HH2	-1.57279	-3.07152	-2.88168	-1.40684	0.25537	3.09705	0.24324	-2.58847
HH3	-1.05553	-2.17940	-2.28045	-1.17705	0.04553	-2.04607	0.03689	2.44805
HH4	-0.61111	-1.29100	-1.31866	-0.69641	-0.00656	-1.18880	-0.01192	1.42407

Table 5.2

The values of the normal form coefficients and parameters ρ_{jk}, used in the expressions for the unfolding parameters, for each of the double Hopf bifurcation points in the (a, τ) plane. Fixed parameter values are $\alpha = 12.457$, $\beta = 0.007095$, $\gamma = 0.641$, $\omega = 2.6\pi$, $b = 1$.

Lines 1-4 divide parameter space into six regions, labelled I-VI in Figure 5.1. There is excellent agreement near HH1 between lines 1 and 2 in (5.2) and the bifurcation curves, taken from Figure 3.2.

The stability of the steady states ① – ④ is found by evaluating the Jacobian J of (B.30), given by,

$$J = \begin{bmatrix} J_{11} & J_{12} \\ J_{21} & J_{22} \end{bmatrix},$$

(5.3)
$$J_{11} = 3a_{11}r_2^2 + a_{12}r_2^2 + \rho_{11}(a - a_c) + \rho_{12}(\tau - \tau_c),$$
$$J_{12} = J_{21} = 2a_{21}r_1r_2,$$
$$J_{22} = a_{21}r_1^2 + 3a_{22}r_2^2 + \rho_{21}(a - a_c) + \rho_{22}(\tau - \tau_c).$$

The analysis leads to the phase portraits in Figure 5.2. Let us consider the qualitative changes in these phase portraits as we move counter-clockwise around the double Hopf point HH1 in Figure 5.1. In region I, only the zero equilibrium ① steady state exists. In agreement with analysis in Section 3, this is stable. A Hopf bifurcation gives rise to the stable in-phase limit cycle ② in region II, and the zero equilibrium becomes a saddle. Moving into region III, an unstable anti-phase limit cycle ③ is born and the zero equilibrium becomes a source. Region IV is a region of bistability of the in-phase and anti-phase limit cycles, together with an unstable quasi-periodic orbit ④. This quasi-periodic orbit then collides with the in-phase limit cycle ② to give the phase portrait in region V, where the anti-phase limit cycle ③ is the only stable steady state. In region VI, the in-phase limit cycle no longer exists, leaving only the stable anti-phase limit cycle ③ and the unstable equilibrium at the origin ①. This limit cycle disappears at a Hopf bifurcation as we move back into region I, and the equilibrium at the origin ① regains stability.

5.2. One-parameter bifurcation diagrams. Apart from obtaining different phase portraits around the double Hopf bifurcation, the normal form (B.30) allows us to plot one-parameter bifurcation diagrams to illustrate the unfolding of the in-phase and anti-phase solutions. These provide a useful means of comparison with numerical results. Figure 5.3
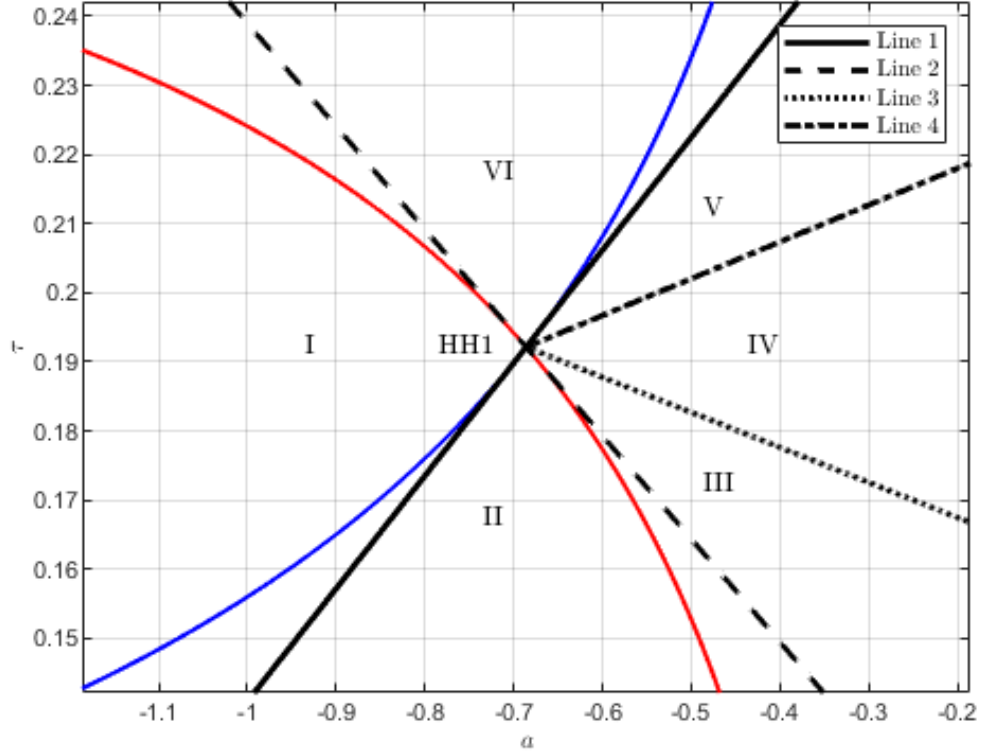
Figure 5.1. *Regions with qualitatively different phase portraits in the vicinity of double Hopf point* HH1: $(a, \tau) = (-0.68609, 0.19214)$. *The blue curve corresponds to* $Re(\lambda^{(i)}) = 0$ *and the red curve to* $Re(\lambda^{(a)}) = 0$. *Lines 1-4 are defined by* (5.2). *Fixed parameter values are* $\alpha = 12.457$, $\beta = 0.007095$, $\gamma = 0.641$, $\omega = 2.6\pi$, $b = 1$.

218   illustrates the one-parameter bifurcation diagrams in a (with $\tau = 0.19214$ from Table 5.1),
219   and τ (with $a = -0.68609$) showing how the double Hopf bifurcation HH1 unfolds. Nu-
220   merical results obtained from DDE-BIFTOOL are compared with the analytic results given
221   by (5.1). The bifurcation diagrams in parameter a show transitions between regions I and
222   IV, and the birth of the two stable limit cycles. In contrast, the bifurcation diagrams in
223   τ show transitions between regions II and VI, showing the destruction of one type of limit
224   cycle, followed by the birth of the other.

225   The centre manifold analysis is valid for small amplitudes near the double Hopf bifur-
226   cation point HH1. Figure 5.3 shows that there is strong agreement between the analytic
227   and numeric solutions within the expected parameter range. It only shows stable solutions.
228   Other solutions will be discussed in the next section.

229   In Appendix C, we give a brief discussion on the possibility, or otherwise, of internal
230   resonances in this problem.
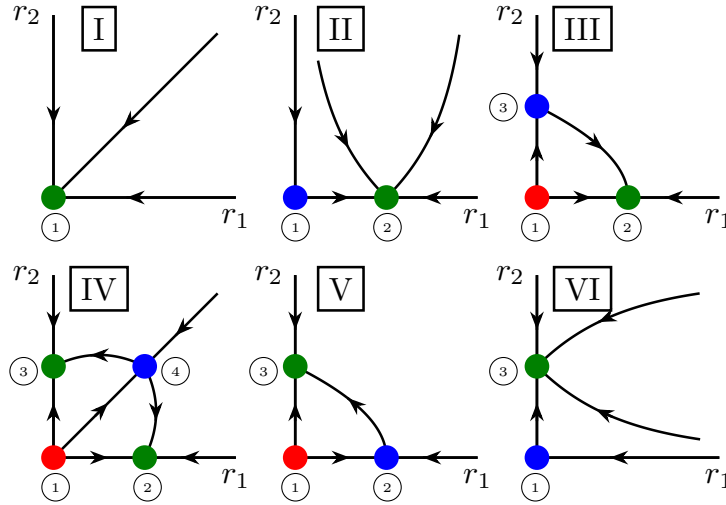
Figure 5.2. *Possible phase portrait topologies around double Hopf point* `HH1`. *Sources, sinks and saddles are illustrated using red, green and blue dots respectively. Roman numerals correspond to the regions in Figure 5.1. Equilibria* ①–④ *are given in* (5.1).

6. Numerical results.

To further analyse the global behaviour of the nonlinear delayed HKB model (2.1), we conducted extensive numerical bifurcation calculations[9]. The results are summarised in Figure 6.1. We computed branches of equilibria and limit cycles using DDE-BIFTOOL [13] and branches of quasi-periodic orbits using the Matlab tool introduced in [11] and further developed in [28].

We analysed the stability of the trivial equilibrium, detected Hopf bifurcations, and continued the branches of Hopf bifurcation in two parameters, a and τ; see the teal branches[10] in Figure 6.1(a). The two branches give rise to the in-phase and anti-phase limit cycles, and their the intersection is the double-Hopf bifurcation point `HH1` at $(a, \tau) = (a_c, \tau_c) = (-0.68609, 0.19214)$. Then, we selected a delay value $\tau = 0.1926$ close to `HH1` and continued the in-phase and anti-phase limit cycles by varying parameter a; these are the black and purple curves, respectively, in Figure 6.1(b), which lie almost on top of one another and above the red quasi-periodic curve[11].

Then, we considered the stability of the in-phase and anti-phase limit cycles. We detected torus bifurcations (orange points) and pitchfork bifurcations (green points), associated with a pair complex and one real characteristic multipliers located on the unit circle of the complex plane, respectively. These bifurcations were continued in two parameters as shown by the orange and green branches in Figure 6.1(a).

---

[9]Code used to obtain these results is available at https://github.com/DomboZoli/Quasi-periodic-package.

[10]These are the red and blue branches in Figure 5.1.

[11]The amplitude measure on the vertical axis is the "root-mean-square value" over the period T: $\|x\| = \sqrt{\frac{1}{T} \int_0^T (x_1^2(t) + x_2^2(t)) \mathrm{d}t}$.
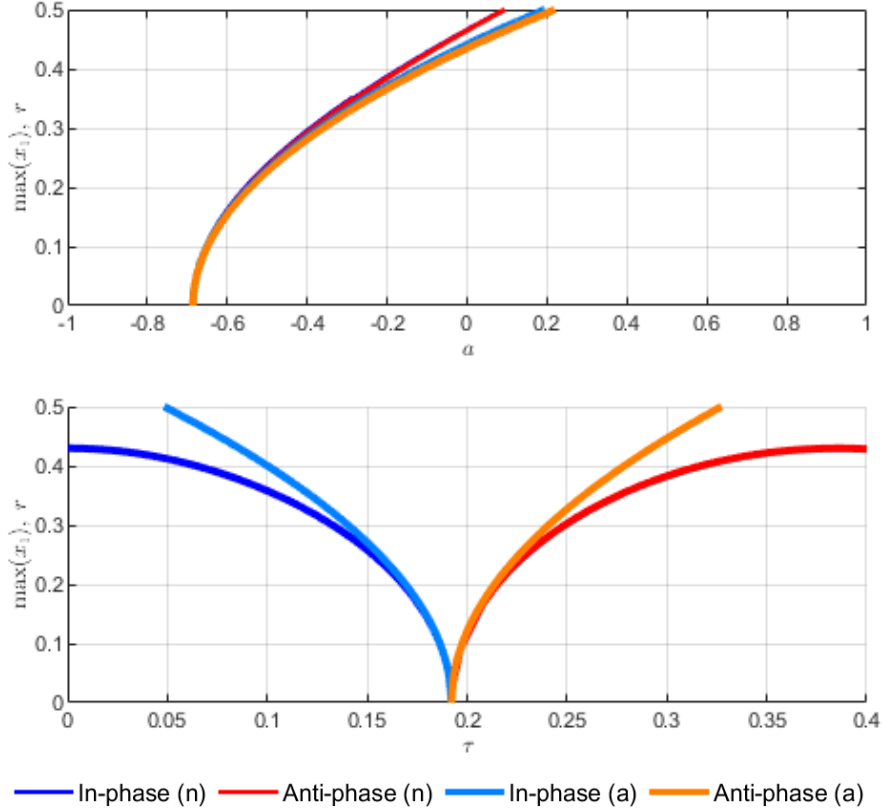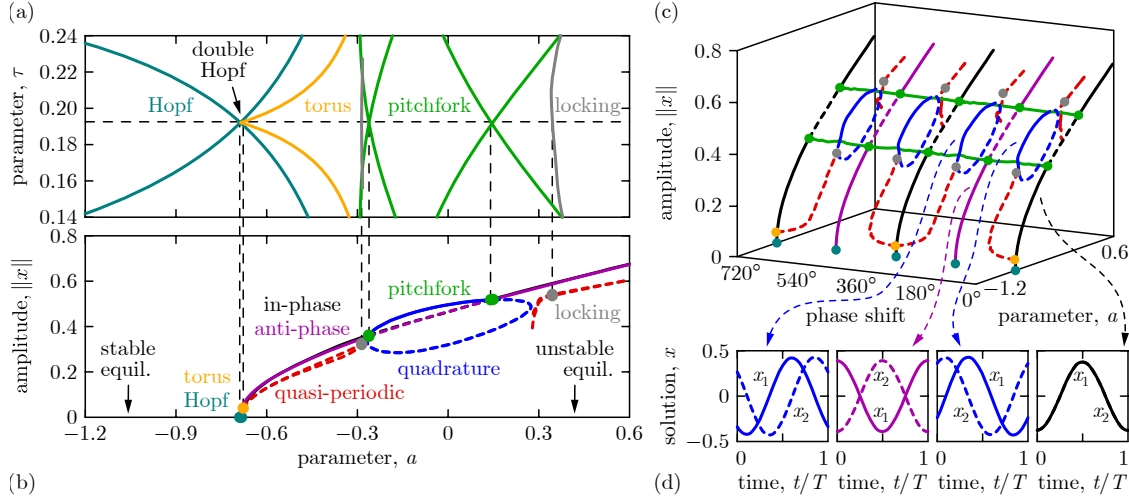
Figure 5.3. *One-parameter bifurcation diagrams in a (with $\tau = 0.19214$ from Table 5.1), and τ (with $a = -0.68609$) for the limit cycles born at HH1. Numerics (n) are compared with the analytic (a) solutions obtained using the normal form given in (B.30). All solutions are stable at the bifurcation point. Fixed parameter values are $\alpha = 12.457$, $\beta = 0.007095$, $\gamma = 0.641$, $\omega = 2.6\pi$, $b = 1$.*

249   The pitchfork bifurcations give rise to additional limit cycles. These solutions are
250 plotted in blue in Figure 6.1(c) as a function of the phase shift[12] between the states x_1 and
251 x_2. The phase shift of the limit cycles changes continuously and sweeps across the entire
252 $[0°, 360°]$ domain. The diagram repeats every $360°$ along the phase shift axis.
253   When the phase shift of these additional limit cycles reaches approximately $90°$ or $270°$,
254 the branch splits into circular branches of limit cycles, where the associated phase shift was
255 observed to be approximately constant $90°$ or $270°$, respectively. We refer to these as *limit*
256 *cycles in phase quadrature*. The circular branches of these solutions can be seen in Figure
257 6.1(b). The in-phase, anti-phase and phase quadrature limit cycles themselves are depicted
258 in Figure 6.1(d) for $a = -0.2$. For these phase quadrature limit cycles, we further observed
259 that the time period is about 4 times the delay, and therefore a special type of symmetry
260 with $x_1(t) \approx x_2(t - \tau)$ or $x_2(t) \approx x_1(t - \tau)$ holds, respectively.
261   The torus bifurcations (orange points in Figure 6.1) give rise to two branches of quasi-

---

[12]Based on the location of the maximum points of $x_1(t)$ and $x_2(t)$.

Figure 6.1. *Numerical bifurcation diagrams of the delayed HKB system* (2.1). *(a) Two-parameter diagram in the* (a, τ) *plane with branches of Hopf, torus, pitchfork bifurcation and 1-1 locking. (b) One-parameter diagram of limit cycles and quasi-periodic orbits against parameter a for $\tau = 0.1926$ (solid line: stable solution, dashed line: unstable solution). (c) One-parameter diagram also indicating the phase shift between x_1 and x_2. (d) In-phase, anti-phase, and phase quadrature periodic orbits at $a = -0.2$. Fixed parameter values are $\alpha = 12.457$, $\beta = 0.007095$, $\gamma = 0.641$, $\omega = 2.6\pi$, $b = 1$.*

periodic orbits (red dashed curves)[13]. The two branches are identical except that x_1 and x_2 are interchanged[14].

The quasi-periodic orbits are associated with two angular frequencies, υ_1 and υ_2, that are close to the frequencies related to the double Hopf point HH1. Accordingly, quasi-periodic orbits are described as a surface (a torus) parameterised by two dimensionless time variables $\theta_1 \in [0, 2\pi]$ and $\theta_2 \in [0, 2\pi]$ associated with υ_1 and υ_2. The quasi-periodic branches are indicated with their phase shift[15] in Figure 6.1(c).

Finally, as the quasi-periodic branch is continued, multiple 1-1 locking states, coloured gray in Figure 6.1, were detected where $\upsilon_1/\upsilon_2 = 1$. At the locking points, the quasi-periodic orbit degrades into the limit cycle in phase quadrature. Near locking, the corresponding torus becomes challenging to compute numerically; see the loss of accuracy along the red curve on the right of Figure 6.1(b).

---

[13]It is not possible to use DDE-BIFTOOL to automatically continue the quasi-periodic orbit from the torus bifurcation that occurs when a limit cycle changes stability. Dombóvári and Stépán [11] point out that saddle-like invariant sets are especially difficult to find for DDEs because the standard trick of tracking solutions along reversed time cannot be used. Their algorithm is not straightforward to implement, and success is dependent on the accuracy of the initial solution profile estimates and on stability properties of the solution in question.

[14]Note that system (2.1) is symmetric in x_1 and x_2, whereas the quasi-periodic orbits branch out from the in-phase solution where $x_1(t) \equiv x_2(t)$.

[15]The amplitude and phase shift were determined based on taking a section $\theta_1 = \mathrm{mod}(\upsilon_1\theta/\upsilon_2, 2\pi)$, $\theta_2 = \mathrm{mod}(\upsilon_2\theta/\upsilon_1, 2\pi)$ of the torus with $\theta \in [0, 2\pi]$, and then using the same amplitude and phase measures for $x_1(t)$ and $x_2(t)$ as for limit cycles with period $T = 2\pi$.

An approximation of the locking point was continued in the (a, τ) plane by establishing a numerical condition on higher harmonics along both dimensionless time coordinates. These harmonics were determined by discrete Fourier transform (DFT), in which the corresponding derivatives with respect to present states, retarded states and parameters were determined analytically to give a well conditioned two parameter continuation scheme. This continuation scheme is detailed in Appendix D. The numerical locking points lie closer to the branch of limit cycles in phase quadrature (blue curve) when $a = -0.29$ than for when $a = 0.34$.

The results in this section provide further information about the global dynamic behaviour of the HKB system (2.1), that could not be obtained by the analytic methods presented in previous sections.

7. Conclusions. In this paper, we discussed the effects of delay on the Haken-Kelso-Bunz (HKB) model [15] of bimanual human motor coordination. We investigated the stability of the trivial solutions in the corresponding linear system (2.4), which can be written as a delayed oscillator where the feedback changes the damping. We discovered Hopf and double Hopf bifurcations in this linear delayed HKB model. We analysed the double Hopf bifurcations in the full HKB system (2.1) by means of centre manifold reduction [15] to calculate the stability of both in-phase and anti-phase limit cycles and quasi-periodic orbits. We verified our results using numerical continuation. In addition, we discovered limit cycles in phase quadrature and 1-1 locking of quasi-periodic orbits. We have shown that in-phase and the anti-phase limit cycles can be replaced by a phase-lagged solution via a pitchfork bifurcation of periodic orbits. This phase lagged solution has transitioned from the quasi-periodic branch which emerges from the double Hopf bifurcation point. This suggests that double frequency transient transitioning is needed to change from in-phase to anti-phase limit cycles, while the phase-lagged solution is reached by increasing the linear coupling coefficient a. The results provide valuable insights into the nonlinear dynamic behaviour of this model, which may help determine the relevance of the delayed HKB system to the application of the mirror game for early diagnosis of disorders such as schizophrenia [37]. Furthermore, we suggest that the methods we have presented may be valuable to assess the corresponding suitability of other delayed models of human motor coordination, such as the variation of the delayed HKB system presented by Słowiński et al. [34], which incorporates a neurologically motivated coupling term.

306   **Appendix A. Stability charts.**   Equation (3.1) has the trivial solution $\eta(t) = 0$. We
307   want to find conditions under which this solution is stable. If this solution becomes unstable
308   via a Hopf bifurcation, we would expect to find finite amplitude limit cycles, corresponding
309   to observable oscillations in the full HKB system (2.1). The characteristic equation of (3.1)
310   is given by

311   (A.1) $$\lambda^2 - (\gamma + a)\lambda + \omega^2 = \mp a\lambda e^{-\lambda\tau}.$$

312   The solution $\eta(t) = 0$ of (3.1) is stable when $\text{Re}(\lambda) < 0$.
313   When $\tau \neq 0$, (A.1) is an exponential polynomial in λ, which has an infinite number of
314   roots (either real or complex conjugate). If *any* of these roots have positive real part, then
315   the steady state $\eta(t) = 0$ is unstable.
316   From Kuang [25, Theorem 1.4, p. 66 & Section 3.3], we know that stability changes
317   (or boundaries) occur when the root with the largest real part is purely imaginary. The
318   locations in parameter space where such roots exist can be found by substituting $\lambda = i\nu$,
319   where $\nu \geq 0$ is real, into (A.1) and equating real and imaginary parts, to give

320   (A.2)
$$\omega^2 - \nu^2 \pm a\nu \sin(\nu\tau) = 0,$$
$$-(\gamma + a)\nu \pm a\nu \cos(\nu\tau) = 0.$$

321   Note that $\nu = 0$ is a solution of (A.2) when $\omega = 0$. Hence we take $\nu > 0$ in the sequel.
322   From (A.2) we obtain a quartic expression in ν,

323   (A.3) $$\nu^4 + \left((\gamma + a)^2 - a^2 - 2\omega^2\right)\nu^2 + \omega^4 = 0,$$

324   which has roots

325   (A.4) $$\nu_{\pm}^2 = \frac{1}{2}\left(a^2 + 2\omega^2 - (\gamma + a)^2 \pm \sqrt{(a^2 + 2\omega^2 - (\gamma + a)^2)^2 - 4\omega^4}\right).$$

326   Since $\nu_{\pm}$ must be real, we have $\lambda_{\pm} = i\nu_{\pm}$, $\nu_+ > \nu_- > 0$ provided that

327   (A.5)
(a) $a^2 + 2\omega^2 - (\gamma + a)^2 > 0,$
(b) $(a^2 + 2\omega^2 - (\gamma + a)^2)^2 > 4\omega^4,$

328   with no solutions otherwise.
329   The real parts of the rightmost eigenvalues either become positive (instability) or neg-
330   ative (stability) when parameters such as τ change. But we do not know in which direction
331   the eigenvalues move. To determine this direction, the sign of the derivative of $\text{Re}\left(\lambda\left(\tau\right)\right)$
332   with respect to τ needs to be found at the point where $\lambda\left(\tau\right)$ is purely imaginary. So we
333   calculate the sign of ρ_{τ}, given by

334   (A.6) $$\rho_{\tau} := \text{Re}\left(\left.\frac{d\lambda}{d\tau}\right|_{\lambda=i\nu}\right).$$

335   It turns out to be more convenient to calculate the inverse of ρ_{τ}, as only its sign matters.
336   By differentiating the characteristic equation (A.1), we obtain

337   (A.7) $$\left(\frac{d\lambda}{d\tau}\right)^{-1} = \frac{\pm\left(2\lambda - (\gamma + a)\right)e^{\lambda\tau} + a}{a\lambda^2} - \frac{\tau}{\lambda}.$$

338 Then substituting the expression for $e^{\lambda\tau}$ obtained from (A.1) into (A.7), and using (A.4),
339 we have
(A.8)

340
$$\operatorname{sign}\rho_\tau = \operatorname{sign}\left[\operatorname{Re}\left(\left(\frac{d\lambda}{d\tau}\right)^{-1}\Bigg|_{\lambda=i\nu_\pm}\right)\right] = \operatorname{sign}\left(\pm\sqrt{(a^2+2\omega^2-(\gamma+a)^2)^2-4\omega^4}\right).$$

341 Thus $\rho_\tau > 0$ (eigenvalues crossing the imaginary axis from left to right with increasing τ)
342 occurs for τ corresponding to ν_+ and $\rho_\tau < 0$ (eigenvalues crossing the imaginary axis from
343 right to left with increasing τ) occurs for τ corresponding to ν_-. We find these values of τ
344 from (A.2), by setting

345 (A.9)
$$\tau_{n,1} = \frac{\theta_1}{\nu_+} + \frac{2n\pi}{\nu_+}$$
$$\tau_{n,2} = \frac{\theta_2}{\nu_-} + \frac{2n\pi}{\nu_-}$$

346 for $n \in \mathbb{Z}$ where $\theta_{1,2} \in [0, 2\pi)$ are given by

347 (A.10)
$$\cos(\theta_1) = \pm\frac{\gamma+a}{a}, \qquad \cos(\theta_2) = \pm\frac{\gamma+a}{a},$$
$$\sin(\theta_1) = \pm\frac{\nu_+^2-\omega^2}{a\nu_+}, \quad \sin(\theta_2) = \pm\frac{\nu_-^2-\omega^2}{a\nu_-}.$$

348   Kuang's theorem [25, Theorem 1.4, p. 66] allows us to consider the eigenvalues λ as a
349 continuous function of τ. Then the stability of the solution $\eta(t) = 0$ of (3.1) for $\tau > 0$ can
350 be found by looking at the stability of the system at $\tau = 0$.
351   If $\eta(t) = 0$ is *stable* when $\tau = 0$, then $\tau_{0,1} < \tau_{0,2}$ because the multiplicity of roots with
352 positive real part cannot become negative. Additionally, we have that

353 (A.11)
$$\tau_{n+1,1} - \tau_{n,1} = \frac{2\pi}{\nu_+} < \frac{2\pi}{\nu_-} = \tau_{n+1,2} - \tau_{n,2}.$$

354 This means that there can only be a finite number of switches between stability and insta-
355 bility. Specifically, there are k switches from stability to instability to stability when

356 (A.12) $\tau_{0,1} < \tau_{0,2} < \tau_{1,1} < \cdots < \tau_{k-1,1} < \tau_{k-1,2} < \tau_{k,1} < \tau_{k+1,1} < \tau_{k,2} < \cdots.$

357   If $\eta(t) = 0$ is *unstable* when $\tau = 0$, then it is either unstable for $\tau > 0$, or a finite
358 number of stability switches occur; k switches from instability to stability to instability
359 *may* occur when

360 (A.13) $\tau_{0,2} < \tau_{0,1} < \tau_{1,2} < \cdots < \tau_{k-1,2} < \tau_{k-1,1} < \tau_{k,1} < \tau_{k,2} < \cdots.$

361 It is straightforward to show that this condition is satisfied for (3.1). This means that
362 stability changes occur according to (A.13) when the system is unstable at $\tau = 0$.
363   Stability charts in parameter spaces (a, τ) and (γ, τ) (Figures 3.2 and 3.3) are obtained
364 by treating (A.9) and (A.10) as functions of a and γ, respectively, and carefully checking

the conditions in (A.12) and (A.13) to see if the resulting curves correspond to stability changes.

The above analysis has to be extended when we examine stability in (γ, a) parameter space for fixed τ. We adapt Kuang's [25] analysis to derive a parameterisation of the $\mathrm{Re}(\lambda) = 0$ curves directly. Rearranging (A.2), we get expressions for a and γ in terms of ν as

$$(A.14) \qquad \begin{aligned} a &= \pm \frac{\nu^2 - \omega^2}{\nu \sin(\nu\tau)}, \\ \gamma &= \frac{\nu^2 - \omega^2}{\nu \sin(\nu\tau)} \left(\cos(\nu\tau) \mp 1 \right), \end{aligned}$$

for $\nu\tau \neq n\pi$, $n \in \mathbb{Z}$.

When $\nu\tau = n\pi$, $n \in \mathbb{Z}$, we have $\nu = \omega$ from the first equation of (A.2). The second equation then gives

$$(A.15) \qquad \gamma = a(\pm(-1)^n - 1) \quad \text{for } \omega \neq 0.$$

We now return to (A.1) and look at the sign of $\mathrm{Re}\left(\left(\frac{d\lambda}{d\gamma} \right)^{-1} \right)$ evaluated on the curves given by (A.14) and (A.15). We find that

$$(A.16) \qquad \mathrm{Re}\left(\left(\frac{d\lambda}{d\gamma} \right)^{-1} \bigg|_{\lambda = i\nu} \right) = 1 + \frac{\omega^2}{\nu^2} - (\gamma + a)\tau =: \xi.$$

In addition it is useful to look at $\frac{da}{d\gamma}$ to see how the change of sign of (A.16) relates to the curves given by (A.14). We find

$$(A.17) \qquad \frac{da}{d\gamma} = \frac{\xi}{\frac{\gamma}{a}\xi - a\tau \sin^2(\nu\tau)},$$

where ξ is defined in (A.16). Hence $\frac{da}{d\gamma} = 0$ if and only if $\xi = 0$, for $a \neq 0$. Therefore, the points in parameter space where the eigenvalues change direction correspond to the turning points of the $\mathrm{Re}(\lambda) = 0$ curves in (γ, a) space.

Appendix B. Centre manifold reduction. First we will outline the method for calculating the normal form of a generic Hopf bifurcation of a DDE system using centre manifold theory and then apply this to find the normal form of the double Hopf bifurcations of the delayed HKB system. The approach given here is outlined by several authors [7, 19, 28]). The detailed theory is discussed by Hale and Verduyn Lunel [16].

This analysis applies to retarded delay differential equations with constant delay $\tau > 0$. Consider a general delay differential equation of this type,

$$\text{(B.1)} \qquad \dot{\mathbf{x}}(t) = \mathbf{g}(\mathbf{x}(t), \mathbf{x}(t-\tau); \mu),$$

where $\mathbf{x} \in \mathbb{R}^n$, $\mathbf{g} : \mathbb{R}^n \times \mathbb{R}^n \times \mathbb{R}^k \to \mathbb{R}^n$, $n, k \in \mathbb{Z}^+$, and $\mu \in \mathbb{R}^k$ and $\tau > 0$ are parameters in the model. We assume that $\mathbf{g}$ is sufficiently smooth for the required computations and that the equation admits an equilibrium solution $\mathbf{x}_*$ which is independent of τ. By shifting the equilibrium to zero and separating linear and nonlinear terms, (B.1) can be written in the form

$$\text{(B.2)} \qquad \dot{\mathbf{x}}(t) = A_0(\mu)\mathbf{x}(t) + A_1(\mu)\mathbf{x}(t-\tau) + \mathbf{f}(\mathbf{x}(t), \mathbf{x}(t-\tau); \mu),$$

where $A_j(\mu) = D_{j+1}\mathbf{g}(\mathbf{x}_*, \mathbf{x}_*; \mu)$ is the Jacobian of $\mathbf{g}$ with respect to its $(j+1)^{\text{th}}$ argument, and

$$\text{(B.3)} \qquad \mathbf{f}(\mathbf{x}(t), \mathbf{x}(t-\tau); \mu) = \mathbf{g}(\mathbf{x}(t), \mathbf{x}(t-\tau); \mu) - A_0(\mu)\mathbf{x}(t) - A_1(\mu)\mathbf{x}(t-\tau).$$

The characteristic equation of (B.1) is then given by

$$\text{(B.4)} \qquad \det(\Delta(\lambda; \mu)) = \det(\lambda I_{n \times n} - A_0(\mu) - A_1(\mu)\mathrm{e}^{-\lambda\tau}) = 0,$$

where $I_{n \times n}$ is the $n \times n$ identity matrix.

The following analysis applies to critical parameter values $\mu = \mu_\mathrm{c}$ where the characteristic equation (B.4) has $m > 0$ roots with zero real part, and the rest of the eigenvalues have negative real parts. We assume that the eigenvalues with zero real part have multiplicity one, which covers single and double Hopf bifurcations.

To make progress with centre manifold construction, the operator differential equation representation of the DDE is required. Writing (B.2) as an evolution equation on the Banach space $\mathcal{B}$ of continuously differentiable functions from $[-\tau, 0]$ to $\mathbb{R}^n$ gives

$$\text{(B.5)} \qquad \dot{\mathbf{x}}_t = \mathcal{A}\mathbf{x}_t + \mathcal{F}(\mathbf{x}_t),$$

where $\mathbf{x}_t \in \mathcal{B}$ is defined by

$$\text{(B.6)} \qquad \mathbf{x}_t(\theta) = \mathbf{x}(t+\theta), \quad \theta \in [-\tau, 0],$$

the linear operator $\mathcal{A}$ is defined by

$$\text{(B.7)} \qquad \mathcal{A}\phi(\theta) = \begin{cases} \frac{\mathrm{d}}{\mathrm{d}\theta}\phi(\theta), & \theta \in [-\tau, 0), \\ A_0(\mu_\mathrm{c})\phi(0) + A_1(\mu_\mathrm{c})\phi(-\tau), & \theta = 0, \end{cases}$$

and the nonlinear operator is

(B.8)
$$\mathcal{F}(\phi)(\theta) = \begin{cases} 0, & \theta \in [-\tau, 0), \\ \mathbf{f}(\phi(0), \phi(-\tau); \mu_c), & \theta = 0. \end{cases}$$

For the nonlinear calculations, it will be useful to define the operators

(B.9)
$$L(\phi) = A_0(\mu_c)\phi(0) + A_1(\mu_c)\phi(-\tau),$$
$$\mathbf{F}(\phi) = \mathbf{f}(\phi(0), \phi(-\tau); \mu_c).$$

The following calculations will also require the dual space $\mathcal{B}^*$ of continuously differentiable functions on $[0, \tau]$ to $\mathbb{R}^{n*}$ (the n-dimensional row vectors), an adjoint operator

(B.10)
$$\mathcal{A}^*\psi(\xi) = \begin{cases} -\frac{d}{d\xi}\psi(\xi), & \xi \in (0, \tau], \\ \psi(0)A_0(\mu_c) + \psi(\tau)A_1(\mu_c), & \xi = 0, \end{cases}$$

where we have assumed $A_0(\mu_c)$ and $A_1(\mu_c)$ are real, and the bilinear form $(\ ,\ ) : \mathcal{B}^* \times \mathcal{B} \to \mathbb{R}$ given by

(B.11)
$$(\psi, \phi) = \psi(0)\phi(0) + \int_{-\tau}^{0} \psi(\sigma + \tau)A_1(\mu_c)\phi(\sigma)d\sigma.$$

The adjoint operator and bilinear form allow a projection of the solution to the DDE at the critical parameter values onto the centre manifold to be constructed. As with the ODE case, a first order approximation is constructed by considering the linear problem. Here the solution space can be decomposed as $\mathcal{B} = \mathcal{C} \bigoplus \mathcal{S}$ where $\mathcal{C}$ is an m-dimensional solution space spanned by the solutions corresponding to the eigenvalues with zero real part, $\mathcal{S}$ is infinite dimensional, and both $\mathcal{C}$ and $\mathcal{S}$ are invariant under the flow of the linear system. These are analogous to the centre and stable eigenspaces for ODEs.

Let $\{\phi_1, \phi_2, \ldots, \phi_m\}$ be the basis for $\mathcal{C}$, with corresponding eigenvalues $\{\lambda_1, \lambda_2, \ldots, \lambda_m\}$. Note that the eigenvalues of $\mathcal{A}$ are the same as the roots of the characteristic equation given by (B.4). It was shown in Appendix A that $\lambda_k = i\nu_k$ with $\nu_k \neq 0$, therefore attention will be restricted to the case where all of the eigenvalues take this form. If $\lambda_k = i\nu_k$ is a root of (B.4), then so is $-i\nu_k$. The eigenvalues are labelled so that $\lambda_{k+1} = -i\nu_k$, where $\nu_k > 0$ and k is odd.

We find the basis for the centre eigenspace as follows. Consider a complex eigenfunction $\Phi_k \in \mathcal{B}$ corresponding to eigenvalue $i\nu_k$ which satisfies $\forall \theta \in [-\tau, 0]$ that

(B.12)
$$\mathcal{A}\Phi_k(\theta) = i\nu_k\Phi_k(\theta).$$

Separating into real and imaginary parts gives

(B.13)
$$\mathcal{A}\phi_k(\theta) = -\nu_k\phi_{k+1}(\theta),$$
$$\mathcal{A}\phi_{k+1}(\theta) = \nu_k\phi_k(\theta),$$

where $\Phi_k(\theta) = \phi_k(\theta) + \mathrm{i}\phi_{k+1}(\theta)$. For convenience, the basis shall be written as an $n \times m$ matrix, defined as

$$(\text{B.14}) \qquad \mathbf{\Phi}(\theta) = \begin{bmatrix} \phi_1(\theta) & \phi_2(\theta) & \cdots & \phi_m(\theta) \end{bmatrix}.$$

Using the definition of $\mathcal{A}$, given by (B.7), it can be shown that

$$(\text{B.15}) \qquad \mathbf{\Phi}'(\theta) = \mathbf{\Phi}(\theta)B,$$

where B is a block diagonal $m \times m$ matrix with blocks

$$(\text{B.16}) \qquad B_k = \begin{bmatrix} 0 & \nu_k \\ -\nu_k & 0 \end{bmatrix}$$

for every pair of complex conjugate eigenvalues $\pm \mathrm{i}\nu_k$. It also follows from the definition of $\mathcal{A}$ that

$$(\text{B.17}) \qquad A_0(\mu_\mathrm{c})\mathbf{\Phi}(0) + A_1(\mu_\mathrm{c})\mathbf{\Phi}(-\tau) = \mathbf{\Phi}(0)B.$$

Solving (B.15) with boundary condition (B.17) gives

$$(\text{B.18}) \qquad \begin{aligned} \phi_k(\theta) &= \mathrm{Re}(\mathrm{e}^{\mathrm{i}\nu_k\theta}\mathbf{v}_k), \\ \phi_{k+1}(\theta) &= \mathrm{Im}(\mathrm{e}^{\mathrm{i}\nu_k\theta}\mathbf{v}_k), \end{aligned}$$

where $\mathbf{v}_k$ satisfies $\Delta(\mathrm{i}\nu_k; \mu_\mathrm{c})\mathbf{v}_k = 0$, and $\Delta(;)$ is given in (B.4).

The basis

$$(\text{B.19}) \qquad \mathbf{\Psi}(\xi) = \begin{bmatrix} \psi_1(\xi) \\ \vdots \\ \psi_m(\xi) \end{bmatrix}$$

for the adjoint can be found in a similar way by deriving and solving

$$(\text{B.20}) \qquad \begin{aligned} \mathbf{\Psi}'(\xi) &= B\mathbf{\Psi}(\xi) \\ \mathbf{\Psi}(0)A_0(\mu_\mathrm{c}) + \mathbf{\Psi}(\tau)A_1(\mu_\mathrm{c}) &= -B\mathbf{\Psi}(0). \end{aligned}$$

Note that the construction of $\mathcal{A}^*$ ensures that the eigenvalues of $\mathcal{A}^*$ are the same as the eigenvalues of $\mathcal{A}$, which is made explicit by considering eigenfunctions of the form $\psi(\xi) = \mathbf{w}\mathrm{e}^{-\lambda\xi}$, $\mathbf{w} \in \mathbb{R}^{n*}$. Here we label the eigenfunction in $\mathcal{B}$ with eigenvalue $\mathrm{i}\nu$ in the same way as the eigenfunction in $\mathcal{B}^*$ with the same eigenvalue.

Solving (B.20) yields

$$(\text{B.21}) \qquad \begin{aligned} \psi_k(\xi) &= \mathrm{Re}(\mathbf{w}_k\mathrm{e}^{-\mathrm{i}\nu_k\xi}), \\ \psi_{k+1}(\xi) &= \mathrm{Im}(\mathbf{w}_k\mathrm{e}^{-\mathrm{i}\nu_k\xi}), \end{aligned}$$

where $\mathbf{w}_k\Delta(\mathrm{i}\nu_k; \mu_\mathrm{c}) = 0$. Using the remaining degrees of freedom, the bases can be chosen such that $(\mathbf{\Psi}, \mathbf{\Phi}) = I_{m \times m}$, where $(\mathbf{\Psi}, \mathbf{\Phi})$ is the matrix with i, j elements (ψ_i, ϕ_j). Note

478 that $\boldsymbol{\Psi}$ may be used to decompose the solution space because for any $\zeta \in \mathcal{S}$, $(\psi_j, \zeta) = 0$
479 for $j = 1, \ldots, m$.
480   Now the nonlinear terms shall be considered. The local centre manifold $W_{\text{loc}}^{\text{c}}$ of the
481 equilibrium at $\mathbf{0}$ can be expressed as the sum of a linear part belonging to $\mathcal{C}$ and a nonlinear
482 part belonging to $\mathcal{S}$,

483 (B.22) $$W_{\text{loc}}^{\text{c}} = \{\phi \in \mathcal{B} \mid \phi = \boldsymbol{\Phi}\mathbf{u} + \mathbf{h}(\mathbf{u})\},$$

484 where $\boldsymbol{\Phi}$ is the basis given by (B.14), $\mathbf{u} \in \mathbb{R}^m$, $\boldsymbol{\Phi}\mathbf{u} \in \mathcal{C}$, $\mathbf{h}(\mathbf{u}) \in \mathcal{S}$ and $\|\mathbf{u}\|$ is sufficiently
485 small. Thus the solutions $\mathbf{x}(t)$ to (B.2) on the centre manifold satisfy $\mathbf{x}(t) = \mathbf{x}_t(0)$ where

486 (B.23) $$\mathbf{x}_t(\theta) = \boldsymbol{\Phi}(\theta)\mathbf{u}(t) + \mathbf{h}(\theta, \mathbf{u}(t)).$$

487 Substituting (B.23) into (B.5) and using (B.15) and (B.17) gives a coupled system of PDEs
488 which must be solved for $\mathbf{u}(t)$ and $\mathbf{h}(\theta, \mathbf{u}(t))$,

489 (B.24)
$$\left(\boldsymbol{\Phi}(\theta) + \frac{\partial \mathbf{h}}{\partial \mathbf{u}}(\theta, \mathbf{u}(t))\right)\dot{\mathbf{u}}(t)$$
$$= \begin{cases} \boldsymbol{\Phi}(\theta)B\mathbf{u}(t) + \frac{\partial \mathbf{h}}{\partial \theta}(\theta, \mathbf{u}(t)), & \theta \in [-\tau, 0), \\ \boldsymbol{\Phi}(0)B\mathbf{u}(t) + L\big(\mathbf{h}(\mathbf{u}(t))\big) + \mathbf{F}\big(\boldsymbol{\Phi}\mathbf{u}(t) + \mathbf{h}(\mathbf{u}(t))\big), & \theta = 0. \end{cases}$$

491 where L and $\mathbf{F}$ are defined in (B.9), and we used the notation $\mathbf{h}(\mathbf{u}(t))$ to refer to $\mathbf{h}$ as a
492 function in $\mathcal{S}$ for given $\mathbf{u}(t)$. The equation for $\mathbf{u}(t)$ can now be derived using the bilinear
493 form (B.11). Firstly, since $\mathbf{h}(\mathbf{u}(t)) \in \mathcal{S}$,

494 (B.25) $$\big(\boldsymbol{\Psi}, \mathbf{h}(\mathbf{u}(t))\big) = 0.$$

495 Taking the partial derivative with respect to $\mathbf{u}$ yields

496 (B.26) $$\left(\boldsymbol{\Psi}, \frac{\partial \mathbf{h}}{\partial \mathbf{u}}(\mathbf{u}(t))\right) = 0.$$

497 Using the equations given in (B.9) and (B.20), it can be shown that

498 (B.27)
$$\boldsymbol{\Psi}(0)L\big(\mathbf{h}(\mathbf{u}(t))\big) + \int_{-\tau}^{0} \boldsymbol{\Psi}(\sigma + \tau)A_1(\mu_{\text{c}})\frac{\partial \mathbf{h}}{\partial \sigma}(\sigma, \mathbf{u}(t))d\sigma,$$
$$= \boldsymbol{\Psi}(0)A_0(\mu_{\text{c}})\mathbf{h}(0, \mathbf{u}(t)) + \boldsymbol{\Psi}(\tau)A_1(\mu_{\text{c}})\mathbf{h}(0, \mathbf{u}(t))$$
$$- \int_{-\tau}^{0} \boldsymbol{\Psi}'(\sigma + \tau)A_1(\mu_{\text{c}})\mathbf{h}(\sigma, \mathbf{u}(t))d\sigma,$$
$$= -B\boldsymbol{\Psi}(0)\mathbf{h}(0, \mathbf{u}(t)) - \int_{-\tau}^{0} B\boldsymbol{\Psi}(\sigma + \tau)A_1(\mu_{\text{c}})\mathbf{h}(\sigma, \mathbf{u}(t))d\sigma,$$
$$= -B\big(\boldsymbol{\Psi}, \mathbf{h}(\mathbf{u}(t))\big)$$
$$= 0.$$

500 Therefore, the bilinear form (B.11) applied to $\mathbf{\Psi}$ and (B.24) gives

501 (B.28) $$\dot{\mathbf{u}}(t) = B\mathbf{u}(t) + \mathbf{\Psi}(0)\mathbf{F}\big(\mathbf{\Phi}\mathbf{u}(t) + \mathbf{h}(\mathbf{u}(t))\big).$$

502 Substituting this into (B.24) gives a system of PDEs for $\mathbf{h}(\theta, \mathbf{u}(t))$,

503 (B.29)
$$\frac{\partial \mathbf{h}}{\partial \mathbf{u}}(\theta, \mathbf{u}(t))\Big(B\mathbf{u}(t) + \mathbf{\Psi}(0)\mathbf{F}\big(\mathbf{\Phi}\mathbf{u}(t) + \mathbf{h}(\mathbf{u}(t))\big)\Big) + \mathbf{\Phi}(\theta)\mathbf{\Psi}(0)\mathbf{F}\big(\mathbf{\Phi}\mathbf{u}(t) + \mathbf{h}(\mathbf{u}(t))\big)$$
$$= \begin{cases} \frac{\partial \mathbf{h}}{\partial \theta}(\theta, \mathbf{u}(t)), & \theta \in [-\tau, 0), \\ L\big(\mathbf{h}(\mathbf{u}(t))\big) + \mathbf{F}\big(\mathbf{\Phi}\mathbf{u}(t) + \mathbf{h}(\mathbf{u}(t))\big), & \theta = 0. \end{cases}$$

504 Standard centre manifold techniques can be used to solve (B.29), expanding $\mathbf{h}(\mathbf{u})$ and $\mathbf{F}$
505 as power series in $\mathbf{u}$ and equating coefficients. Substituting the result into (B.28) and
506 expanding the right-hand side in powers of $\mathbf{u}$ gives the equation for the flow on the centre
507 manifold. To compute the normal form for the double Hopf bifurcation, however, it is
508 not necessary to solve the PDE, because the coefficients of expressions up to and including
509 cubic terms allow the normal form for the bifurcation to be identified directly using formulas
510 available in the literature, which we now discuss.
511   A double Hopf bifurcation is a codimension-2 bifurcation, meaning it requires two
512 parameters $\mu_{1,2}$ to analyse its unfolding. Let $\mu_1 = \mu_{1c}$ and $\mu_2 = \mu_{2c}$ at the bifurcation
513 point. The normal form of the double Hopf bifurcation can be expressed in polar form in
514 terms of two amplitudes r_1, r_2, and two phase angles φ_1, φ_2 [28] as

515 (B.30)
$$\dot{r}_1 = b_1 r_1 + \big(a_{11} r_1^2 + a_{12} r_2^2\big) r_1,$$
$$\dot{r}_2 = b_2 r_2 + \big(a_{21} r_1^2 + a_{22} r_2^2\big) r_2,$$

516 and

517 (B.31)
$$\dot{\varphi}_1 = \nu_1 + c_{11} r_1^2 + c_{12} r_2^2,$$
$$\dot{\varphi}_2 = \nu_2 + c_{21} r_1^2 + c_{22} r_2^2,$$

518 where $r_{1,2} \in \mathbb{R}$, $r_{1,2} > 0$ and $\varphi_{1,2} \in \mathbb{R}$. The parameters a_{jk} and c_{jk}, $j, k \in \{1, 2\}$ are
519 known as the normal form coefficients. These can be calculated using formulae derived by
520 [24] from the coefficients of $\mathbf{u}$ in (B.28) after (B.29) has been solved for $\mathbf{h}$ and the right-
521 hand side has been expanded in powers of $\mathbf{u}$. The coefficients b_j, $j \in \{1, 2\}$ are unfolding
522 parameters.[16] The unfolding parameters can be approximated by linear functions of the
523 bifurcations parameters [28],

524 (B.32)
$$b_1 = \rho_{11}(\mu_1 - \mu_{1c}) + \rho_{12}(\mu_2 - \mu_{2c}),$$
$$b_2 = \rho_{21}(\mu_1 - \mu_{1c}) + \rho_{22}(\mu_2 - \mu_{2c}),$$

525 where

526 (B.33)
$$\rho_{jk} = \text{Re}\left(\left.\frac{\partial \lambda}{\partial \mu_k}\right|_{\mathrm{i}\nu_j}\right),$$

---

[16]Not to be confused with the parameter b in the delayed HKB equation, the unfolding parameters will always have 1 or 2 as a subscript.

527 which can be calculated by differentiating the characteristic equation (B.4); see Appen-
528 dix A. The focus of our analysis will be on the amplitudes r_1, r_2, which allow the existence
529 and stability of the limit cycle near the bifurcation point to be investigated.

530   **Appendix C. Resonances.**

531   The analysis presented in this paper assumes no resonant phenomena. We address the
532   possibility of internal resonances in the delayed HKB model (2.1) here. The system has a
533    $k_1 : k_2$ resonance if $\frac{\nu_1}{\nu_2} = \frac{k_1}{k_2}$ for $k_1, k_2 \in \mathbb{Z}^+$. If k_1 and k_2 are relatively prime integers and
534    $k_1 + k_2 > 4$ then the resonance is said to be weak, and no change to the normal form is
535   required because the leading-order nonlinearities remain the same as for the non-resonant
536   case [27]. A change to the normal form is required if $k_1 + k_2 \leq 4$.

537   By comparing $\nu^{(i)}$ and $\nu^{(a)}$ at the double Hopf points, it is straightforward to show
538   that if resonance occurs, it will be weak. The possibility of weak resonance should be
539   investigated so that we can distinguish between resonant and non-resonant behaviour.
540   Examples of weakly resonant and non-resonant behaviour that can arise at double Hopf
541   bifurcations are presented by Ma et al. [27].

542   Ma et al. [27] outline a method for finding the parameter values for which a $k_1 : k_2$ reso-
543   nant double Hopf bifurcation occurs. In the case of the delayed HKB equation, determining
544   whether the double Hopf bifurcations found for specific parameter values correspond to res-
545   onances is not straightforward due to the complex expression for the frequencies ν, given
546   by (A.4). The relevant equations for finding the double Hopf bifurcations were solved
547   numerically. Without analytic expressions for the parameter values at the double Hopf
548   point, it cannot be determined with certainty that resonance is not present. However, by
549   comparing $\nu^{(i)}$ and $\nu^{(a)}$, $k_1 : k_2$ resonance can be ruled out in a finite number of cases. For
550   example, for each of the double Hopf bifurcations found in the previous section, there is
551   no $k_1 : k_2$ resonance for $k_1, k_2 \in \{1, 2, \ldots, 1000\}$.

552   Experimentally, there is no evidence of resonance phenomena, nor are resonance phe-
553   nomena mentioned by Słowiński et al. [36] who used the same parameter values. If ex-
554   periments in the future suggest the existence of resonant phenomena for physiologically
555   relevant parameter values, the exact parameter values which cause this can be found using
556   the approach outlined by Ma et al. [27]. However, without evidence of the phenomenon,
557   resonance need not be discussed further here.

Appendix D. Two-parameter continuation of invariant tori near locking.

The quasi-periodic orbits have been computed using the 2D collocation algorithm in [11, 28], based on the method introduced in [31]. In what follows, we describe some of the trade-offs associated with this method when it is used to continue quasi-periodic orbits near locking.

The numerical continuation of quasi-periodic branches involves significantly higher errors when passing through resonances [32]. This is the case in Figure 6.1 near the 1:1 strong resonance (locking) points (grey dots) where the quasi-periodic orbit collapses to the period-one limit cycle in phase quadrature (note the loss of accuracy along the red dashed lines). We can write the governing equation (2.1) in the form $\dot{\mathbf{u}} = \mathbf{f}(\mathbf{u}, \mathbf{u}_\tau, \boldsymbol{\mu})$ with $\mathbf{u} = \begin{bmatrix} x_1 & x_2 & \dot{x}_1 & \dot{x}_2 \end{bmatrix}^\top$ and $\mathbf{u}_\tau := \mathbf{u}(t - \tau)$. Computing and storing the invariant tori profiles $\mathbf{u}(\theta_1, \theta_2)$ at a given bifurcation parameter $\boldsymbol{\mu}$ becomes increasingly difficult as the required resolution increases. The numerical computation of quasi-periodic branches breaks down near the 1:1 strong resonance as it becomes increasingly difficult to satisfy the invariance relations [31]

(D.1)
$$v_1 \frac{\partial \mathbf{u}}{\partial \theta_1} + v_2 \frac{\partial \mathbf{u}}{\partial \theta_2} - \mathbf{f}(\mathbf{u}, \mathbf{u}_\tau, \boldsymbol{\mu}) = \mathbf{0},$$
$$\mathbf{u}(0, \theta_2) - \mathbf{u}(2\pi, \theta_2) = \mathbf{0},$$
$$\mathbf{u}(\theta_1, 0) - \mathbf{u}(\theta_1, 2\pi) = \mathbf{0},$$
$$\left\langle \frac{\partial \mathbf{u}}{\partial \theta_k}, \mathbf{u} \right\rangle = 0, \qquad k = 1, 2,$$
$$\Gamma(\mathbf{u}, \mathbf{u}_\tau, v_k, \boldsymbol{\mu}) = 0, \qquad k = 1, 2.$$

The function Γ is given below. Pseudo-arclength [10] continuation is used to solve (D.1), supplemented with arclength condition. Equation (D.1) is evaluated over a Chebyshev quadrature [31]. It is not entirely clear why the breakdown of the numerical scheme arises around strong locking [32].

Since the locking point is unreachable by continuation, approximate two-parameter $\boldsymbol{\mu} := [a\ \tau]^\top$ near-locking branches - grey curves in Figure 6.1(a) - were continued using the following discretization of the invariance scheme (D.1). For this two-parameter continuation, the function Γ is defined based on the fact that the numerical scheme will eventually disperse close to the 1:1 resonance, with ripples propagating higher than the Pth harmonics on the invariant torus profile given by

(D.2)
$$\mathbf{u}(\theta_1, \theta_2) := \mathsf{C}_{i=1,j=1}^{N,M} \mathbf{u}_{i,j}(\theta_1, \theta_2),$$
$$\mathbf{u}_{i,j}(\theta_1, \theta_2) = \sum_{p=0}^{P} \sum_{q=0}^{P} \mathbf{u}_{i,j,p,q} P_{p,q}(\epsilon_i(\theta_1), \epsilon_j(\theta_2)),$$
$$P_{p,q}(\epsilon_i(\theta_1), \epsilon_j(\theta_2)) := P_p(\epsilon_i(\theta_1)) P_q(\epsilon_j(\theta_2)),$$
$$P_k(\epsilon) := \prod_{m=0, m \neq k}^{P} \frac{P\epsilon - m}{k - m}, \quad \epsilon_i(\theta_1) := \frac{\theta_1 - \theta_{1,i}}{\Delta\theta_1}, \quad \epsilon_j(\theta_2) := \frac{\theta_2 - \theta_{2,j}}{\Delta\theta_2},$$

over the mesh $\theta_{1,i} := (i-1)\Delta\theta_1$ and $\theta_{2,j} := (j-1)\Delta\theta_2$, where C denotes the concatenation of segmented 2D polynomial surfaces $\mathbf{u}_{i,j}$.

The different harmonics k and l in the spectrum are defined on the velocity profile $\dot{\mathbf{u}}_k$ of the invariant tori over both coordinates as

(D.3) $$\mathbf{U}_{1,k}(\theta_2) := \int_0^{2\pi} \dot{\mathbf{u}}(\theta_1,\theta_2)\mathrm{e}^{\mathrm{i}k2\pi\theta_1}\mathrm{d}\theta_1, \quad \mathbf{U}_{2,l}(\theta_1) := \int_0^{2\pi} \dot{\mathbf{u}}(\theta_1,\theta_2)\mathrm{e}^{\mathrm{i}l2\pi\theta_2}\mathrm{d}\theta_2.$$

The main idea behind continuing near the locking curve is to lock on the relative error Δ between the main harmonics and the cumulated higher ones as

(D.4) $$\Gamma := \left(\frac{\sum_{K=1,2} S_{K,1} - \sum_{K=1,2}\sum_{L=P+1}^{N} S_{K,L}}{\sum_{K=1,2} S_{K,1}} \right)^2 - \Delta^2,$$

with

(D.5) $$S_{1,k} := \int_0^{2\pi} \mathbf{U}_{1,k}^{\mathsf{H}}(\theta_2)\mathbf{U}_{1,k}(\theta_2)\mathrm{d}\theta_2, \quad S_{2,l} := \int_0^{2\pi} \mathbf{U}_{2,l}^{\mathsf{H}}(\theta_1)\mathbf{U}_{2,l}(\theta_1)\mathrm{d}\theta_1.$$

Corresponding derivatives can be computed using the chain rule and Newton-Raphson correction can be performed quite effectively.

598   **REFERENCES**

599 [1] D Avitabile, P Słowiński, B Bardy, and K Tsaneva-Atanasova. Beyond in-phase and anti-phase
600   coordination in a model of joint action. *Biological Cybernetics*, 110:201–216, 2016.
601 [2] A Banerjee and V K Jirsa. How do neural connectivity and time delays influence bimanual coordina-
602   tion? *Biological Cybernetics*, 96:265–278, 2006.
603 [3] S J Bhatt and C S Hsu. Stability criteria for second-order dynamical systems with time lag. *Trans-
604   actions ASME Journal of Applied Mechanics*, 33(1):113–118, 1966.
605 [4] M M Bosschaert, S G Janssens, and Y A Kuznetsov. Switching to nonhyperbolic cycles from codi-
606   mension two bifurcations of equilibria of delay differential equations. *SIAM Journal on Applied
607   Dynamical Systems*, 19(1):252–303, 2020.
608 [5] J Bourbousson, C Seve, and T McGarry. Space-time coordination dynamics in basketball: Part 1.
609   Intra- and inter-couplings among player dyads. *Journal of Sports Sciences*, 28(3):339–347, 2010.
610 [6] J J Buchanan and Y U Ryu. One-to-one and polyrhythmic temporal coordination in bimanual circle
611   tracing. *Journal of Motor Behavior*, 38(3):163–184, 2006.
612 [7] S A Campbell. Calculating centre manifolds for delay differential equations using Maple$^{\text{TM}}$. In D E
613   Gilsinn, T Kalmár-Nagy, and B Balachandran, editors, *Delay Differential Equations*. Springer,
614   Boston, MA, 2009.
615 [8] J F Cass and S J Hogan. Two dimensionless parameters and a mechanical analogue for the HKB
616   model of motor coordination. *Biological Cybernetics*, 115(4):343–364, 2021.
617 [9] J J Collins and I N Stewart. Coupled nonlinear oscillators and the symmetries of animal gaits. *Journal
618   of Nonlinear Science*, 3(1):349–392, 1993.
619 [10] E J Doedel, W Govaerts, and Y A Kuznetsov. Computation of periodic solution bifurcations in ODEs
620   using bordered systems. *SIAM Journal on Numerical Analysis*, 41(2):401–435, 2003.
621 [11] Z Dombovari and G Stépán. On the bistable zone of milling processes. *Philosophical Transactions of
622   the Royal Society A*, 373(20140409), 2015.
623 [12] R Duarte, D Araujo, K Davids, B Travassos, V Gazimba, and J Sampaio. Interpersonal coordina-
624   tion tendencies shape 1-vs-1 sub-phase performance outcomes in youth soccer. *Journal of Sports
625   Sciences*, 30(9):871–877, 2012.
626 [13] K Engelborghs, T Luzyanina, and D Roose. Numerical bifurcation analysis of delay differential
627   equations using DDE-BIFTOOL. *ACM Transactions on Mathematical Software*, 28(1):1–21, 2002.
628 [14] J Guckenheimer and P Holmes. *Nonlinear Oscillations, dynamical systems, and bifurcations of vector
629   fields*. Springer, New York, NY, 1983.
630 [15] H Haken, J A S Kelso, and H Bunz. A theoretical model of phase transitions in human hand move-
631   ments. *Biological Cybernetics*, 51:347–356, 1985.
632 [16] J K Hale and S M Verduyn Lunel. *Introduction to Functional Differential Equations*, volume 99 of
633   *Applied Mathematical Sciences*. Springer-Verlag, New York, NY, 1993.
634 [17] B D Hassard, N D Kazarinoff, and Y H Wan. *Theory and Applications of Hopf bifurcations*, volume 41
635   of *London Mathematical Society Lecture Note Series*. Cambridge University Press, Cambridge,
636   1981.
637 [18] C S Hsu and S J Bhatt. Stability charts for second-order dynamical systems with time lag. *Transactions
638   ASME Journal of Applied Mechanics*, 33(1):119–124, 1966.
639 [19] T Kalmár-Nagy, G Stépán, and F C Moon. Subcritical Hopf bifurcation in the delay equation model
640   for machine tool vibrations. *Nonlinear Dynamics*, 26:121–142, 2001.
641 [20] B A Kay, J A S Kelso, E L Saltzman, and G S Schöner. Space-time behavior of single and bimanual
642   rhythmical movements: Data and limit cycle model. *Journal of Experimental Psychology: Human
643   Perception and Performance*, 13:178–190, 1987.
644 [21] J A S Kelso. On the oscillatory basis of movement. *Bulletin of the Psychonomic Society*, 18(2):63–63,
645   1981.
646 [22] J A S Kelso. *Dynamic patterns: The self-organization of brain and behavior*. MIT press, 1995.
647 [23] J A S Kelso. The Haken-Kelso-Bunz (HKB) model: from matter to movement to mind. *Biological
648   Cybernetics*, 115(4):305–322, 2021.
649 [24] E Knobloch. Normal form coefficients for the nonresonant double Hopf bifurcation. *Physics Letters*

        A, 116(8):365–369, 1986.

[25] Y Kuang. *Delay differential equations with applications in population dynamics*. Academic Press, inc.,
        1st edition, 1993.

[26] M Lombardi, D Liuzza, and M di Bernardo. Generation and classification of individual behaviours for
        virtual players control in motor coordination tasks. *European Control Conference (ECC)*, pages
        2374–2379, 2018.

[27] S Ma, Q Lu, and Z Feng. Double Hopf bifurcation for van der Pol-Duffing oscillator with parametric
        delay feedback control. *Journal of Mathematical Analysis and Applications*, 338:993–1007, 2008.

[28] T G Molnár, Z Dombóvári, T Insperger, and G Stépán. On the analysis of the double Hopf bifur-
        cation in machining processes via centre manifold reduction. *Proceedings of the Royal Society A*,
        473(20170502), 2017.

[29] L Noy, E Dekel, and U Alon. The mirror game as a paradigm for studying the dynamics of two people
        improvising motion together. *PNAS*, 108(52):20947–20952, 2011.

[30] C Peper, A Ridderikhoff, A Daffertshofer, and P J Beek. Explanatory limitations of the HKB model:
        Incentives for a two-tired model of rhythmic interlimb coordination. *Human Movement Science*,
        23:673–697, 2004.

[31] D Roose and R Szalai. Continuation and bifurcation analysis of delay differential equations. In Bernd
        Krauskopf, Hinke M. Osinga, and Jorge Galán-Vioque, editors, *Numerical Continuation Methods
        for Dynamical Systems: Path following and boundary value problems*, pages 359–399. Springer
        Netherlands, Dordrecht, 2007.

[32] F Schilder, H M Osinga, and W Vogt. Continuation of quasi-periodic invariant tori. *SIAM Journal
        on Applied Dynamical Systems*, 4(3):459–488, 2005.

[33] J Sieber, K Engelborghs, T Luzyanina, G Samaey, and D Roose. DDE-BIFTOOL v. 3.1.1 Manual -
        Bifurcation analysis of delay differential equations. Available at http://arxiv.org/abs/1406.7144
        (05/04/2017).

[34] P Słowiński, S Al-Ramadhani, and K Tsaneva-Atanasova. Neurologically motivated coupling functions
        in models of motor coordination. *SIAM Journal on Applied Dynamical Systems*, 19(1):208–232,
        2020.

[35] P Słowiński, F Alderisio, C Zhai, Y Shen, P Tino, C Bortolon, D Capdevielle, L Cohen, M Kho-
        ramshahi, A Billard, R Salesse, M Gueugnon, L Marin, B Bardy, M di Bernardo, S Raffard, and
        K Tsaneva-Atanasova. Unravelling socio-motor biomarkers in schizophrenia. *NPJ Schizophrenia*,
        3, 2017.

[36] P Słowiński, K Tasaneva-Atanasova, and B Krauskopf. Effects of time-delay in a model of intra-
        and inter-personal motor coordination. *European Physical Journal Special Topics*, 225:2591–2600,
        2016.

[37] M Varlet, L Marin, S Raffard, R Schmidt, D Capdevielle, J P Boulenger, J Del-Monte, and B G
        Bardy. Impairments of social motor coordination in schizophrenia. *PLoS ONE*, 7(1):e29772, 2012.

[38] A Washburn, R W Kallen, C A Coey, K Shockley, and M J Richardson. Harmony from chaos?
        Perceptual-motor delays enhance behavioral anticipation in social interaction. *Journal of Experi-
        mental Psychology: Human Perception and Performance*, 41(4):1166–1177, 2015.

[39] C Zhai, F Alderisio, P Słowiński, and K Tsaneva-Atanasova. Design and validation of a virtual player
        for studying interpersonal coordination in the mirror game. *IEEE Transactions on Cybernetics*,
        48(3):1018–1029, 2018.

[40] C Zhai, Y He, and C-K Zhang. Design and validation of feedback controller for social motor coordi-
        nation with time-varying delays. *Control Engineering Practice*, 109, 2021.